Mathematical Biology

Adjusting the range of cell–cell communication enables fine-tuning of cell fate patterns from checkerboard to engulfing

Simon Schardt[1] · Sabine C. Fischer[1]

Abstract

During development, spatio-temporal patterns ranging from checkerboard to engulfing occur with precise proportions of the respective cell fates. Key developmental regulators are intracellular transcriptional interactions and intercellular signaling. We present an analytically tractable mathematical model based on signaling that reliably generates different cell type patterns with specified proportions. Employing statistical mechanics, We derived a cell fate decision model for two cell types. A detailed steady state analysis on the resulting dynamical system yielded necessary conditions to generate spatially heterogeneous patterns. This allows the cell type proportions to be controlled by a single model parameter. Cell–cell communication is realized by local and global signaling mechanisms. These result in different cell type patterns. A nearest neighbor signal yields checkerboard patterns. Increasing the signal dispersion, cell fate clusters and an engulfing pattern can be generated. Altogether, the presented model allows us to reliably generate heterogeneous cell type patterns of different kinds as well as desired proportions.

✉ Simon Schardt
schardt.simon@outlook.de

Sabine C. Fischer
sabine.fischer@uni-wuerzburg.de

1   Center for Computational and Theoretical Biology, University of Würzburg, Würzburg, Germany

⌀ Springer

1 Introduction

Cell fate decisions play an essential role in establishing cellular function during development. In this process, previously indeterminate cells specify themselves into one of several different cell types. In many cases, there is a strong correlation between gene expression patterns and subsequent cell fate. Therefore, it is necessary to understand the dynamics of different genes to unravel the secrets of differentiation.

One prime example of this differentiation process is the differentiation towards neural and epidermal cells in *Drosophila*. Characteristically, epidermal cell progenitors express high levels of transmembrane protein Notch, whereas neural progenitors express low levels of the same (Heitzler and Simpson 1991; Sternberg 1993). A similar example is found in the inner cell mass (ICM) of the preimplantation mouse embryo. There, the transcription factors (TFs) NANOG and GATA6 have been identified as the earliest markers for the segregation of the ICM into epiblast and primitive endoderm cells, respectively (Mitsui et al. 2003; Schrode et al. 2014). Apart from the spatial cell fate distribution, the correct cell fate ratio is also of particular interest (Saiz et al. 2016, 2020; Schröter et al. 2015).

In mathematical models, cell fate decisions are often described by systems of ordinary differential equations (ODE) based on a gene regulatory network (GRN) (reviewed in Torii 2012). At the single cell level, toggle switches as models of interactions of two genes have been investigated in great detail. These represent mutual inhibition of two proteins (Cherry and Adler 2000), which in some cases are combined with auto-activation (Huang et al. 2007). As a result, three stable steady states arise with regard to gene expression that represent the different cell fates. It depends on the initial conditions which state a cell will be attracted to. At the tissue level, experimental studies hint towards the importance of paracrine signals with regards to differentiation (Nichols et al. 2009; Yamanaka et al. 2010).

Lateral interaction models have already found their way into the current research landscape. For the Delta-Notch signaling pathway, patterns of alternating cell types have been reconstructed (Collier et al. 1996). For the mouse embryo, models including cell–cell communication due to fibroblast growth factor signaling have been employed to create similar salt-and-pepper/checkerboard patterns (Bessonnard et al. 2014; Tosenberger et al. 2017). So far, these studies are concerned with an averaged nearest neighbor signal, i.e. cells do not communicate beyond their nearest neighbor. Further studies suggest that in fact cell fate patterning in the mouse embryo is the result of a complex interplay of cell signaling, cell division, cell sorting and apoptosis (Morris et al. 2010a, b; Nissen et al. 2017).

Mathematical modeling allows untangling the individual components and investigating their pattern formation potential. It was previously shown that cell division alone yields cell fate clusters (Liebisch et al. 2020). Simulations of cells sorting due to differential adhesion have been shown to generate engulfing patterns (Revell et al. 2019). This resembles the result of the minimization of the total contact energy (Emily and François 2007). Here, we focus on the potential of intercellular signaling. In addition to nearest neighbor signaling, we consider signaling that can reach further across a tissue. This builds upon previous ideas for *Drosophila* (Chen et al. 2014; Cohen

Fig. 1 Illustration of the GRN considered in this study. Inside the cell, U and V inhibit each other. In addition to that, they activate themselves. The signal S is a factor that is influenced by the other cells in the tissue. It inhibits U and activates V

Inhibition

Activation
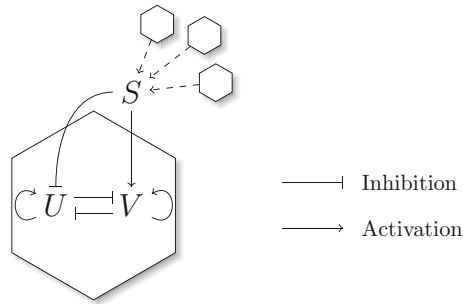
et al. 2010; de Joussineau et al. 2003) as well as the mouse embryo (Raina et al. 2021; Stanoev et al. 2021).

Based on methods from statistical mechanics (Bintu et al. 2005a, b; Garcia et al. 2011), we derived a model describing the temporal development of the expressions of two genes. A generalized signal incorporates external influences on cell fate decisions. Performing a detailed stability analysis of the ODE system, we obtained necessary conditions in the form of a parameter interval to always generate a mixture of two different cell types in a tissue. Numerical simulations for an averaged nearest neighbor signal as well as a distance-based signal demonstrate the potential of our model to establish different spatial cell fate patterns ranging from checkerboard via clustering to engulfing patterns. To quantify the different resulting patterns, we employed individualized pair correlation functions (PCFs). A cell type proportion analysis revealed which proportions our model can create, but also which restrictions there are. Our work introduces an easy to control mathematical model for gene expression and our analysis results provide insight into signaling driven pattern formation and cell type proportioning.

2 Protein interaction model

One of the aims of this study is to numerically simulate cell differentiation influenced by cell–cell communication. The cells will be fixed on an irregular grid regulating their concentration of key TFs internally, while also being influenced by surrounding cells. In this section, we will go through the details of transcriptional regulation based on a simple and generalized model. This will be followed by the derivation of TF binding probabilities based on the methods from Bintu et al. (2005a), Bintu et al. (2005b) and Garcia et al. (2011) which allow us to describe transcriptional regulation on the level of the DNA. Finally, this will be applied to a simple system of two different TFs U and V together with an external signal S describing the cell–cell communication. To this end, we consider a GRN characterized by the mutual inhibition of U and V, as well as their auto-activation and the signal S activating V and inhibiting U (Fig. 1). We consider this to be a general GRN for the cell fate decisions between two cell types, resembling similar GRNs from Huang et al. (2007) or Stanoev et al. (2021).

2.1 Gene regulation

To describe the dynamical system underlying transcriptional regulation, we consider two basic assumptions:

1. Transcription determines the production of new protein.
2. Decay describes the lifetime of the protein.

These assumptions are translated into a generic ODE describing the nondimensionalized concentration $u = u(t)$ of the protein U over time:

$$\frac{du}{dt} = r_u p_u - \gamma_u u. \tag{1}$$

The second term is the exponential decay with decay rate γ_u. The first term describes the rate of transcription of the corresponding gene. Here, p_u denotes the probability that RNA polymerase (RNAP) is bound to the promoter of the gene that is associated with U. The production rate r_u describes how much protein can be produced while RNAP is bound.

2.2 Binding probability

Following (Bintu et al. 2005a, b; Garcia et al. 2011), we consider the different binding events of a GRN. However, we assume that the auto-activatory part of U is dominant, such that the base activity of the RNA polymerase will be neglected. This means that the production of U mainly depends on its binding close to its own promoter. Now the system can be in two different states. Either U is bound or it is not. First we count the number of possibilities how these states might arise. We divide our space into Ω different lattice sites, then U and u are related via $U = u\Omega$. The binomial coefficients yield the number of possible states

$$\text{Number of unbound states:} \qquad \frac{\Omega!}{U!(\Omega - U)!} \tag{2}$$

$$\text{Number of bound states:} \qquad \frac{\Omega!}{(U-1)!(\Omega - U + 1)!} \tag{3}$$

Assuming different energies whether a protein is unbound $\varepsilon_u^{unbound}$ or bound ε_u^{bound}, the two states have total energies

$$\varepsilon^{unbound} = U\varepsilon_u^{unbound}, \tag{4}$$

$$\varepsilon^{bound} = (U-1)\varepsilon_u^{unbound} + \varepsilon_u^{bound}. \tag{5}$$

Using Boltzmann statistics, the energy of the two states enables us to describe the probability that the system is in either of these states via $e^{-\beta\varepsilon^{unbound}}$ and $e^{-\beta\varepsilon^{bound}}$. The partition function is given by the sum of all possible Boltzmann weights over every microstate, i.e.

🖄 Springer

$$Z_{total} = \sum_{\text{microstates}} e^{-\beta\varepsilon_{\text{microstate}}} \tag{6}$$

$$= \frac{\Omega!}{U!(\Omega-U)!}e^{-\beta\varepsilon^{unbound}} + \frac{\Omega!}{(U-1)!(\Omega-U+1)!}e^{-\beta\varepsilon^{bound}} \tag{7}$$

$$= Z^{unbound} + Z^{bound}. \tag{8}$$

Using the partition function, we are able to calculate the binding probability p_u by the ratio of bound states Z^{bound} and all states combined $Z^{unbound} + Z^{bound}$ as

$$p_u = \frac{Z^{bound}}{Z^{unbound} + Z^{bound}}. \tag{9}$$

Assuming $\Omega \gg U$, we use the approximation $\frac{\Omega!}{(\Omega-U)!} \approx \Omega^U$. We divide the numerator and denominator of (9) by $Z^{unbound}$ and define the energy difference $\Delta\varepsilon_u := \beta(\varepsilon_u^{bound} - \varepsilon_u^{unbound})$ to obtain

$$p_u = \frac{Z^{bound}/Z^{unbound}}{1 + Z^{bound}/Z^{unbound}} = \frac{\frac{U}{\Omega}e^{-\Delta\varepsilon_u}}{1 + \frac{U}{\Omega}e^{-\Delta\varepsilon_u}}. \tag{10}$$

For simplicity, we introduce the energy coefficient $\eta_u := e^{-\Delta\varepsilon_u}$ and use $u = U/\Omega$ to get again the volume fractions. This leads to

$$p_u = \frac{\eta_u u}{1 + \eta_u u}. \tag{11}$$

With Eq. (11) we have presented a binding probability solely based on the assumption that there is a difference between bound and unbound states. In general, TF-DNA interactions are much more complex and involve further effects like TF diffusion along the genome (Gerland et al. 2002). In our simplified model however, we only need statistical weights, e.g. η_u, which manipulate the likelihood of binding events. The terms "binding energy" and "energy difference" we use throughout this study should therefore be regarded with caution.

2.3 Interactions

The crucial parts in transcriptional regulation are the interactions between constituents. In the following, we consider that an additional species V interacts with the promoter associated with U. This results in a system, with the following microstates: The binding energy differences remain as before with an additional factor for the interaction $\eta_{uv} = e^{-\Delta\varepsilon_{uv}}$. The binding probabilities for U and V are then given by

$$p_u = \frac{\eta_u u + \eta_u \eta_v \eta_{uv} uv}{1 + \eta_u u + \eta_v v + \eta_u \eta_v \eta_{uv} uv}. \tag{12}$$

Binding event	Number of states
U unbound V unbound	$\dfrac{\Omega!}{U!V!(\Omega!-U-V)!}$
U bound V unbound	$\dfrac{\Omega!}{(U-1)!V!(\Omega!-U-V+1)!}$
U unbound V bound	$\dfrac{\Omega!}{U!(V-1)!(\Omega!-U-V+1)!}$
U bound V bound	$\dfrac{\Omega!}{(U-1)!(V-1)!(\Omega!-U-V+2)!}$

The advantage or disadvantage given by the interaction energy difference now determines the nature of the interaction. For $\eta_{uv} = 1$, (12) can be simplified using factorization to obtain

$$p_u = \frac{\eta_u u + \eta_u \eta_v uv}{1 + \eta_u u + \eta_v v + \eta_u \eta_v uv} = \frac{\eta_u u(1 + \eta_v v)}{(1 + \eta_u u)(1 + \eta_v v)} = \frac{\eta_u u}{1 + \eta_u u}. \tag{13}$$

The binding probability reduces to the case without interaction. Consequently, the cases where $\eta_{uv} \neq 1$ describe binding probabilities that are either lower or higher than the case with no interaction, hence

- $\eta_{uv} = 0$ ⇔ $\Delta\varepsilon_{uv} = \infty$: complete inhibition/blocking
- $\eta_{uv} < 1$ ⇔ $\Delta\varepsilon_{uv} > 0$: inhibition
- $\eta_{uv} = 1$ ⇔ $\Delta\varepsilon_{uv} = 0$: no interaction
- $\eta_{uv} > 1$ ⇔ $\Delta\varepsilon_{uv} < 0$: activation.

Case $\eta_{uv} = 0$ was listed separately, because it represents a special case of inhibition in which U and V cannot be bound at the same time. To improve readability, we use only lowercase letters in the following to denote both the concentrations in terms of ODEs and the actual proteins in the case of binding.

2.4 Describing the cell fate decision between two fates

We imagine a system, where two antagonistic proteins u and v are the deciding factors for the decision of a cell's fate. Both u and v are assumed to be dominantly auto-activating, such that the base activity of the RNAP can be neglected. Additionally, they will be influenced by an external signal s. Following the derivations from Sects. 2.2 to 2.3, this leads to a generalized binding probability for u

$$p_u = \frac{\eta_u u + \eta_u \eta_v \eta_{uv} uv + \eta_u \eta_s \eta_{us} us + \eta_u \eta_v \eta_s \eta_{uvs} uvs}{1 + \eta_u u + \eta_v v + \eta_u \eta_v \eta_{uv} uv + \eta_u \eta_s \eta_{us} us + \eta_v \eta_s \eta_{vs} vs + \eta_u \eta_v \eta_s \eta_{uvs} uvs} \tag{14}$$

Interchanging the letters u and v in (14) yields the binding probability p_v. As before, each summand describes a different binding event, using their individual coefficients

η_u, η_v, and η_s but also the interaction coefficients η_{uv}, η_{us} and η_{vs}. Since we have three constituents u, v and s, we incorporate the possibility that all three of them are bound with interaction coefficient η_{uvs}.

We simplify Eq. (14) by putting it into biological context. We already mentioned the antagonistic nature of our proteins, i.e. u and v mutually inhibit each other. We use a blocking type of inhibition such that the promoter associated with u is not active as soon as v is bound in the vicinity of u's promoter and vice-versa. We can also interpret this as u not being able to bind, if v is already bound, mathematically expressed via $\eta_{uv} = 0$. Finally, the external signal s influences u and v in different ways. It activates v by cooperatively binding with v, i.e. $\eta_{vs} \geq 1$. At the same time, u is inhibited by s and the cooperative binding of u and s leading to $\eta_{us} = 0$ and $\eta_{uvs} = 0$. We assume that for both promoters, the respective energy coefficients are equal. Summarizing the above, we obtain

$$\eta_{uv} = \eta_{us} = \eta_{uvs} = 0, \qquad \eta_{vs} \geq 1 \iff -\Delta\varepsilon_{vs} > 0. \tag{15}$$

Using (15) in (14), we obtain the binding probability for u

$$p_u = \frac{\eta_u u}{1 + \eta_v v(1 + \eta_s \eta_{vs} s) + \eta_u u + \eta_s s}. \tag{16}$$

Analogously, we can use the same approach for the binding probability of v to find

$$p_v = \frac{\eta_v v(1 + \eta_s \eta_{vs} s)}{1 + \eta_v v(1 + \eta_s \eta_{vs} s) + \eta_u u + \eta_s s}. \tag{17}$$

With the expressions for (16) and (17), we can finally get back to the base model for transcriptional regulation (1). So far, we have described the transcriptional regulation of a single cell. However, by extending the system to N different cells, we can also describe a tissue of identically functioning cells. Combined, this leads to the following system of ODEs

$$\begin{aligned}
\frac{du_i}{dt} &= r_u \frac{\eta_u u_i}{1 + \eta_v v_i(1 + \eta_s \eta_{vs} s_i) + \eta_u u_i + \eta_s s_i} - \gamma_u u_i \\
\frac{dv_i}{dt} &= r_v \frac{\eta_v v_i(1 + \eta_s \eta_{vs} s_i)}{1 + \eta_v v_i(1 + \eta_s \eta_{vs} s_i) + \eta_u u_i + \eta_s s_i} - \gamma_v v_i, \qquad i = 1, ..., N.
\end{aligned} \tag{18}$$

We note that so far, we have very little assumptions on the signal s. However, it should be noted that the signal is meant to be provided by the surrounding cells in the tissue. This means that the absorbed signals of each cell s_i are provisionally considered as a generalized function of the expression values of all cells such that

$$\boldsymbol{s} : \mathbb{R}^N \times \mathbb{R}^N \to \mathbb{R}^N : (\boldsymbol{u}, \boldsymbol{v}) \mapsto \boldsymbol{s}(\boldsymbol{u}, \boldsymbol{v}). \tag{19}$$

Thus, Eq. (18) present a coupled system of ODEs.

<div align="right">🌱 Springer</div>

3 Steady state analysis

3.1 Existence of steady states

In order to get a better understanding of our ODE system, we want to delve further into the resulting steady states of the system. This means, we consider

$$\frac{du_i}{dt} = 0 = \frac{dv_i}{dt}.$$

Consequently, we get

$$\frac{\eta_u u_i}{1 + \eta_u v_i (1 + \eta_s \eta_{vs} s_i) + \eta_u u_i + \eta_s s_i} = \frac{\gamma_u}{r_u} u_i, \tag{20}$$

$$\frac{\eta_v v_i (1 + \eta_s \eta_{vs} s_i)}{1 + \eta_v v_i (1 + \eta_s \eta_{vs} s_i) + \eta_u u_i + \eta_s s_i} = \frac{\gamma_v}{r_v} v_i. \tag{21}$$

When rearranging (20) and (21), we find two possible solutions for u_i and v_i, respectively. These solutions are

$$u_i = \begin{cases} 0 \\ \frac{r_u}{\gamma_u} - \frac{1 + \eta_v v_i (1 + \eta_s \eta_{vs} s_i) + \eta_s s_i}{\eta_u} \end{cases} \quad \text{and} \quad v_i = \begin{cases} 0 \\ \frac{r_v}{\gamma_v} - \frac{1 + \eta_u u_i + \eta_s s_i}{\eta_v (1 + \eta_s \eta_{vs} s_i)} \end{cases} . \tag{22}$$

The steady states of our ODE system have to fulfill (20) and (21) together. Thus, we look at every possibly combinations of pairs u_i and v_i from (22) to obtain four different steady states. For three of the steady states, we can get either no expression of u and v or high expression of one TF and none for the other:

$$u_i = 0, \qquad\qquad v_i = 0 \tag{23}$$

$$u_i = \frac{r_u}{\gamma_u} - \frac{1 + \eta_s s_i}{\eta_u}, \qquad\qquad v_i = 0 \tag{24}$$

$$u_i = 0, \qquad\qquad v_i = \frac{r_v}{\gamma_v} - \frac{1 + \eta_s s_i}{\eta_v (1 + \eta_s \eta_{vs} s_i)}. \tag{25}$$

These steady states share the lower bound 0. Additionally, a rough estimate for an upper bound is given by the ratios of reproduction and decay r_u/γ_u and r_v/γ_v. For parameter combinations such that

$$\frac{r_u}{\gamma_u} \gg \frac{1}{\eta_u}, \quad \frac{r_v}{\gamma_v} \gg \frac{1}{\eta_v} + \frac{\eta_s}{\eta_v} s_i, \tag{26}$$

the left hand sides of the inequalities provide a reliable estimate for the steady state values.

The fourth steady state is an oddity that arises by combining the non-zero solutions for u_i and v_i from (22). When combined, the corresponding variables u_i and v_i cancel out and we find the relation

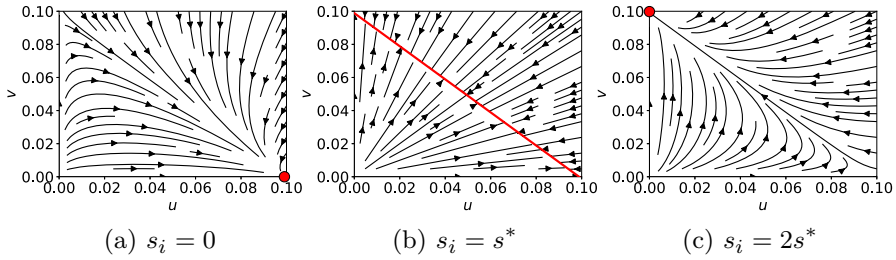(a) $s_i = 0$ (b) $s_i = s^*$ (c) $s_i = 2s^*$

Fig. 2 Streamline phase portraits of ODE system (18) for a single cell and three different values for s_i. Arrows show the path from the initial condition towards the respective steady states. States (24) and (25) are visualized as a single red dot, whereas the infinite steady states resulting from (28) are depicted as a red line

$$\eta_v(1 + \eta_s\eta_{vs}s_i) = \eta_u\frac{r_u\gamma_v}{r_v\gamma_u}. \tag{27}$$

This also leaves our system to be over-determined and the values of u_i and v_i cannot further be identified. However, by using (27) in the steady state solution $v_i \neq 0$ in (22), we obtain the following state:

$$u_i + \frac{r_u\gamma_v}{r_v\gamma_u}v_i = \frac{r_u}{\gamma_u} - \frac{1 + \eta_s s_i}{\eta_u}. \tag{28}$$

Isolating s_i in Eq. (27) leads to a critical signal value

$$s^* = \frac{r_u\gamma_v\eta_u - r_v\gamma_u\eta_v}{r_v\gamma_u\eta_v\eta_s\eta_{vs}}, \tag{29}$$

for which this steady state will always occur. This critical signal value s^* contains all of the model parameters and resembles a difference of the statistical weights η_u and η_v normalized by the remaining model parameters. Furthermore, s^* is responsible for a switching behavior in our system (Fig. 2). For values below or above s^*, a cell ends up in states (24) (u^+v^-) and (25) (u^-v^+), respectively. At exactly s^*, u and v move towards the straight line defined by (28) with no unique steady state. Altogether, we have successfully identified the relevant steady states (23)–(25) of our ODE system (18) as well as the condition to force a switch in the cell's fate.

3.2 Linear stability analysis

In the following sections, we investigate the steady states in further detail. We employ linear stability analysis to determine the parameter regime that allows us to find a desired steady state for the overall system. At the single cell level, we rule out (23), since it is not relevant to cell fate specification. At the tissue level, we distinguish between homogeneous and heterogeneous steady states. A homogeneous equilibrium state consists of cells of a single type only. This means that either all of the cells in the tissue are in state (24) (u^+v^-) or all of them are in state (25) (u^-v^+). Throughout

this study, we aim for states of the tissue where two different cell types co-occur, i.e. heterogeneous equilibrium states. Therefore, we aim at excluding the homogeneous steady states. We follow the definition of linear stability for an ODE system

$$\frac{dx_i}{dt} = f(x), \quad i = 1, ..., N.$$

We say, an ODE system is linearly stable in x^*, if its linearization matrix $L^{ODE} = f'(x^*)$ has only eigenvalues with negative real part. Using the N-dimensional identity matrix I_N, we can write the linearization matrix of (18) as

$$L^{ODE} = \begin{pmatrix} r_u A_{uu} - \gamma_u I_N & r_u A_{uv} \\ r_v A_{uv} & r_v A_{vv} - \gamma_u I_N \end{pmatrix}, \tag{30}$$

Using the chain rule, the block matrices A_{xy}, $x, y \in \{u, v\}$ can be written in terms of the partial derivatives

$$A_{uu} = \frac{\partial p_u}{\partial u} + \frac{\partial p_u}{\partial s}\frac{\partial s}{\partial u}, \qquad A_{uv} = \frac{\partial p_u}{\partial v} + \frac{\partial p_u}{\partial s}\frac{\partial s}{\partial v}, \tag{31}$$

$$A_{vu} = \frac{\partial p_v}{\partial u} + \frac{\partial p_v}{\partial s}\frac{\partial s}{\partial u}, \qquad A_{vv} = \frac{\partial p_v}{\partial v} + \frac{\partial p_v}{\partial s}\frac{\partial s}{\partial v}, \tag{32}$$

where we define $\frac{\partial p_u}{\partial u} := \left(\frac{\partial p_u}{\partial u_j}(u_i, v_i, s_i)\right)_{i,j=1,...,N}$. The other block matrices are defined analogously. For our purposes, we only need to focus on the following derivatives

$$\frac{\partial}{\partial u_j} p_u(u_i, v_i, s_i) = \begin{cases} \frac{\eta_u(1+\eta_v v_i(1+\eta_s \eta_{vs} s_i)+\eta_s s)}{(1+\eta_v v_i(1+\eta_s \eta_{vs} s_i)+\eta_u u_i+\eta_s s_i)^2}, & \text{if } i = j \\ 0, & \text{if } i \neq j \end{cases} \tag{33}$$

$$\frac{\partial}{\partial v_j} p_u(u_i, v_i, s_i) = \begin{cases} -\frac{\eta_v \eta_u u_i(1+\eta_s \eta_{vs} s_i)}{(1+\eta_v v_i(1+\eta_s \eta_{vs} s_i)+\eta_u u_i+\eta_s s_i)^2}, & \text{if } i = j \\ 0, & \text{if } i \neq j \end{cases} \tag{34}$$

$$\frac{\partial}{\partial u_j} p_v(u_i, v_i, s_i) = \begin{cases} -\frac{\eta_v \eta_u v_i(1+\eta_s \eta_{vs} s_i)}{(1+\eta_v v_i(1+\eta_s \eta_{vs} s_i)+\eta_u u_i+\eta_s s_i)^2}, & \text{if } i = j \\ 0, & \text{if } i \neq j \end{cases} \tag{35}$$

$$\frac{\partial}{\partial v_j} p_v(u_i, v_i, s_i) = \begin{cases} -\frac{\eta_v(1+\eta_s \eta_{vs} s_i)(1+\eta_u u_i+\eta_s s_i)}{(1+\eta_v v_i(1+\eta_s \eta_{vs} s_i)+\eta_u u_i+\eta_s s_i)^2}, & \text{if } i = j \\ 0, & \text{if } i \neq j \end{cases} \tag{36}$$

$$\frac{\partial}{\partial s_i} p_u(u_i, v_i, s_i) = -\frac{\eta_u \eta_s u_i(1+\eta_v \eta_{vs} v_i)}{(1+\eta_v v_i(1+\eta_s \eta_{vs} s_i)+\eta_u u_i+\eta_s s_i)^2} \tag{37}$$

$$\frac{\partial}{\partial s_i} p_v(u_i, v_i, s_i) = \frac{\eta_v \eta_s v_i(\eta_{vs}+\eta_u \eta_{vs} u_i-1)}{(1+\eta_v v_i(1+\eta_s \eta_{vs} s_i)+\eta_u u_i+\eta_s s_i)^2}. \tag{38}$$

As usual, the eigenvalues of matrix L^{ODE} are defined as the roots of the characteristic polynomial

$$\chi(\lambda) = \det(L^{ODE} - \lambda I_{2N}), \tag{39}$$

where I_{2N} denotes the identity matrix in $2N$ dimensions. At first glance, this determinant seems impossible to calculate. However, when inserting the respective steady states, we are able to reduce the matrix tremendously.

3.3 Excluding steady state (23)

In the following, we elaborate on how to exclude the first steady state (23) as stable solution for our ODE system (18). Without loss of generality, we assume $u_1 = 0 = v_1$.

This way, in row $N + 1$ all entries but one of the matrix $L^{ODE} - \lambda I_{2N}$ become 0. The remaining entry with index $(N + 1, N + 1)$ is

$$r_v \frac{\partial}{\partial v_1} p_v(0, 0, s_1) - \gamma_v - \lambda = r_v \eta_v \frac{1 + \eta_s \eta_{vs} s_1}{1 + \eta_s s_1} - \gamma_v - \lambda. \tag{40}$$

Laplace expansion then enables us to write the determinant of the whole matrix as a product of (40) and the determinant of the remaining submatrix. Thus, it suffices to focus on the first eigenvalue given by

$$r_v \eta_v \frac{1 + \eta_s \eta_{vs} s_1}{1 + \eta_s s_1} - \gamma_v - \lambda \overset{!}{=} 0.$$

This translates to the eigenvalue λ being

$$\lambda = r_v \eta_v \frac{1 + \eta_s \eta_{vs} s_1}{1 + \eta_s s_1} - \gamma_v.$$

Now, $\lambda > 0$ yields

$$\eta_v > \frac{\gamma_v}{r_v} \frac{1 + \eta_s s_1}{1 + \eta_s \eta_{vs} s_1}.$$

Although the signal thus far has not been further specified, we propose a realistic physical representation by assuming $s_i \geq 0$. Furthermore, we consider an activation of v by the signal s, i.e. $\eta_{vs} > 1$ and therefore, inequality

$$\eta_v > \frac{\gamma_v}{r_v} \tag{41}$$

and consequently

$$-\Delta\varepsilon_v > \ln\left(\frac{\gamma_v}{r_v}\right) \tag{42}$$

provide the necessary condition for instability. The exclusion of this steady state strengthens our focus on (24) and (25), which represent the two different cell types u^+v^- and u^-v^+, respectively.

3.4 Instability of tissue-wide homogeneous steady state (24)

With steady states (24) and (25), we aim to find a parameter region for which we achieve a heterogeneous steady state, i.e. we get a tissue with a mixture of cells in the two states. To this end, we derive conditions for instability of the homogeneous steady state. We start with state (24) and set $u_i = \frac{r_u}{\gamma_u} - \frac{1 + \eta_s s_i}{\eta_u}$ and $v_i = 0$ for all i. Inserting these expressions into the derivatives (33)–(38) results in a simplification of L^{ODE}. Since (35) and (38) are zero for every i, j, the off-diagonal block matrix $A_{vu} = \mathbf{0}$. This means the determinant is given by the product of the determinants of the block matrices on the diagonal. Again, since (38) is zero, A_{vv} becomes a diagonal matrix with diagonal entries

$$(A_{vv})_i = \frac{\eta_v(1 + \eta_s \eta_{vs} s_i)}{1 + \eta_u u_i + \eta_s s_i}, \qquad i = 1, ..., N. \tag{43}$$

Inserting u_i yields

$$(A_{vv})_i = \frac{\gamma_u}{r_u} \frac{\eta_v}{\eta_u}(1 + \eta_s \eta_{vs} s_i), \qquad i = 1, ..., N. \tag{44}$$

Using this, we determine N factors of the characteristic polynomial

$$\chi(\lambda) = \det(r_u A_{uu} - (\gamma_u + \lambda)I_N)\det(r_v A_{vv} - (\gamma_v + \lambda)I_N) \tag{45}$$

$$= \det(r_u A_{uu} - (\gamma_u + \lambda)I_N)\left[\prod_{i=1}^{N}\gamma_u \frac{r_v \eta_v}{r_u \eta_u}(1 + \eta_s \eta_{vs} s_i) - \gamma_v - \lambda\right] \tag{46}$$

and N eigenvalues are given by the second factor in (46). For instability, it is sufficient that only one of these is greater than zero. In other words, this results in the inequality

$$\gamma_u \frac{r_v \eta_v}{r_u \eta_u}(1 + \eta_s \eta_{vs} s_i) > \gamma_v.$$

After appropriate rearranging, we obtain

$$\eta_u < \eta_v \frac{r_v \gamma_u}{r_u \gamma_v}(1 + \eta_s \eta_{vs} \max_i s_i) \tag{47}$$

as a sufficient condition for our parameters. At this point, the general case cannot be simplified further. Depending on the cell–cell interaction and therefore the incoming signal s_i, one can find an even more accurate description of this relation. Alternatively, we can formulate this condition in terms of energy differences as

$$- \Delta \varepsilon_u < - \Delta \varepsilon_v + \ln \left(1 + e^{-\Delta \varepsilon_s - \Delta \varepsilon_{vs}} \max_i s_i \right) + \ln \left(\frac{r_v \gamma_v}{r_u \gamma_v} \right), \qquad (48)$$

which allows us to see the maximum allowed deviation of the difference between $\Delta \varepsilon_u$ and $\Delta \varepsilon_v$. Keep in mind that for this condition, we only relied on the first N eigenvalues. In truth, this condition might be even more relaxed than what we derived.

3.5 Instability of tissue-wide homogeneous steady state (25)

We set $u_i = 0$ and $v_i = \frac{r_v}{\gamma_v} - \frac{1 + \eta_s s_i}{\eta_v (1 + \eta_s \eta_{vs} s_i)}$. Using the same approach as before, we find that (34) and (37) are zero for all i, j and thus $A_{uv} = \mathbf{0}$. In addition to that, we get a diagonal matrix for A_{uu}. For $u_i = 0$, its diagonal entries are

$$(A_{uu})_i = \frac{\eta_u}{1 + \eta_v v_i (1 + \eta_s \eta_{vs} s_i) + \eta_s s_i}, \qquad i = 1, ..., N. \qquad (49)$$

Inserting v_i yields

$$(A_{uu})_i = \frac{\gamma_v}{r_v} \frac{\eta_u}{\eta_v} \frac{1}{1 + \eta_s \eta_{vs} s_i}, \qquad i = 1, ..., N. \qquad (50)$$

As before, this allows us to determine N factors of the characteristic polynomial

$$\chi(\lambda) = \det (r_u A_{uu} - (\gamma_u + \lambda) I_N) \det (r_v A_{vv} - (\gamma_v + \lambda) I_N) \qquad (51)$$

$$= \left[\prod_{i=1}^{N} \gamma_v \frac{r_u}{r_v} \frac{\eta_u}{\eta_v} \frac{1}{1 + \eta_s \eta_{vs} s_i} - \gamma_u - \lambda \right] \det (r_v A_{vv} - (\gamma_v + \lambda) I_N). \qquad (52)$$

We exploit again the instability condition that any eigenvalue must be positive and find the inequality

$$\eta_u > \frac{r_v \gamma_u}{r_u \gamma_v} \eta_v (1 + \eta_s \eta_{vs} s_i). \qquad (53)$$

This yields another condition for η_u. As before, it is necessary to fulfill this inequality for a single value s_i, i.e. the minimum of all possible signal values suffices in that regard. Hence, we get

$$\eta_u > \frac{r_v \gamma_u}{r_u \gamma_v} \eta_v (1 + \eta_s \eta_{vs} \min_i s_i). \qquad (54)$$
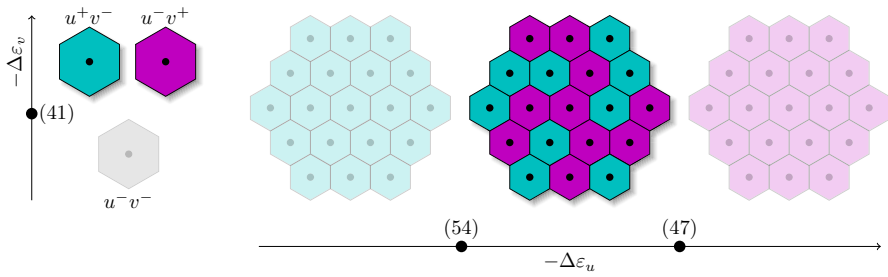
Fig. 3 Illustration of the different steady states at the single cell level (left) and the tissue level (right). The states we are aiming for are highlighted with higher opacity. Nodes and their corresponding number on the axes reference the relevant equation for the transition from one state to another

Again, we write this in terms of energy differences

$$-\Delta\varepsilon_u > -\Delta\varepsilon_v + \ln\left(1 + e^{-\Delta\varepsilon_s - \Delta\varepsilon_{vs}} \min_i s_i\right) + \ln\left(\frac{r_v\gamma_u}{r_u\gamma_v}\right). \tag{55}$$

3.6 Steady state summary

The stability conditions (48) and (55) define an interval

$$\Delta\varepsilon_{min} < -\Delta\varepsilon_u < \Delta\varepsilon_{max} \tag{56}$$

with

$$\Delta\varepsilon_{min} := -\Delta\varepsilon_v + \ln\left(1 + e^{-\Delta\varepsilon_s - \Delta\varepsilon_{vs}} \min_i s_i\right) + \ln\left(\frac{r_v\gamma_u}{r_u\gamma_v}\right), \tag{57}$$

$$\Delta\varepsilon_{max} := -\Delta\varepsilon_v + \ln\left(1 + e^{-\Delta\varepsilon_s - \Delta\varepsilon_{vs}} \max_i s_i\right) + \ln\left(\frac{r_v\gamma_u}{r_u\gamma_v}\right). \tag{58}$$

The reproduction rates r_u, r_v and decay rates γ_u, γ_v shift this interval by $\ln\left(\frac{r_u\gamma_v}{r_v\gamma_u}\right)$. The length of the interval is determined by the minimum and maximum signal values combined with the associated energy differences $-\Delta\varepsilon_s$ and $-\Delta\varepsilon_{vs}$. The results of our stability analysis are summarized in Fig. 3. At the single cell level, we are able to exclude u^-v^- cells using inequality (42). Therefore, at the tissue level, we can distinguish between three different states. The stability interval (56) yields the exact parameter regime for the transition of the homogeneous states to the heterogeneous ones. These elegant lower and upper bounds for $-\Delta\varepsilon_u$ incorporate every parameter in our ODE system (18). Finally, we know that the lower bound in (56) is associated with the homogeneous u^-v^+ state, whereas the upper bound is associated with the homogeneous u^+v^- state. Therefore, we expect a monotonous increase in the number of u^+v^- cells as the energy difference $-\Delta\varepsilon_u$ increases.
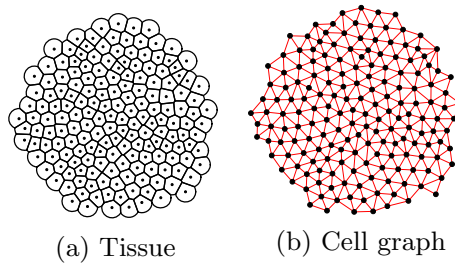
(a) Tissue   (b) Cell graph

Fig. 4 Visualization of a tissue with 177 cells (**a**) and its corresponding cell graph (**b**). Black lines represent the cell membranes. The cell centroids are shown as black dots in both pictures. Red lines represent the edges, which provide information about which cells are in contact with each other (color figure online)

4 Tissue organization

4.1 Cell graph

Cells are represented by two-dimensional points in space with a fixed radius which is equal for all cells. The Delaunay cell graph provides a reliable indication of the neighborhood relationships of the cells (Schmitz et al. 2017). Therefore, we initialize our graph G using the Delaunay triangulation. If the Euclidean distance between two cells exceeds the sum of their two radii, then the edge is removed from G, i.e. only cells in direct contact with each other are connected via an edge in G (Fig. 4). Edge weights are collectively set to 1. We then define the cell distance d_{ij} as the length of the shortest path between cells i and j. In this work, we chose to perform the simulations on a two-dimensional tissue for easier visualisation. However, the same approach has already been successfully applied in three spatial dimensions (Dirk et al. 2022).

4.2 Pair correlation function

Cell differentiation patterns in our case are the result of two different cell types arising in a tissue. Patterns with the same condition have already been quantified using pair correlation functions (PCFs) (Binder and Simpson 2013). We use a similar approach to quantify our patterns with a PCF depending on the cell distances d_{ij}. The PCF relates the number of cell pairs of equal type to the random chance of picking two cells of equal type. Thus, it enables us to find accumulations of cell types at given distances towards each other. This requires counting different types of cell pairings for certain distances. In order to describe the PCF mathematically, we first introduce various sets. The set S_k describes all the cell pairs (i, j) found at a distance d_{ij}. Similarly, S_k^u denotes the set of all u^+v^- cell pairs with distance k. Analogously, S_k^v is defined for u^-v^+ cell pairs. Finally, the two sets T^u and T^v contain all u^+v^- cells and u^-v^+ cells respectively. In mathematical notation, we write

$$S_k = \left\{ (i, j) \in \mathbb{N}^2 : d_{ij} = k, \ 1 \leq i, j \leq N \right\}, \tag{59}$$

$$S_k^u = \{(i, j) \in S_k : i \text{ and } j \text{ are } u^+v^- \text{ cells}\}, \tag{60}$$

$$S_k^v = \{(i, j) \in S_k : i \text{ and } j \text{ are } u^-v^+ \text{ cells}\}, \tag{61}$$

$$T^u = \{i \in \mathbb{N} : i \text{ is } u^+v^- \text{ cell } 1 \le i \le N\}, \tag{62}$$

$$T^v = \{i \in \mathbb{N} : i \text{ is } u^-v^+ \text{ cell } 1 \le i \le N\}. \tag{63}$$

In the next step, we want to find the proportions of the number of equal pairings by looking at the ratio of cell pairs of equal type and pair of any type. We denote the cardinality, i.e. the number of elements, of a set S by $|S|$. Thus, we calculate the proportions $r_{uu}(k)$ of u^+v^- pairs at distance k as well as the proportions $r_{vv}(k)$ of u^-v^+ pairs at distance k via

$$r_{uu}(k) = \frac{|S_k^u|}{|S_k|} \quad \text{and} \quad r_{vv}(k) = \frac{|S_k^v|}{|S_k|}. \tag{64}$$

The goal is to relate these proportions with the probability of randomly picking two cells of equal type. For this, we need the total number of u^+v^- cells T^u and u^-v^+ cells T^v. The chance of picking one u^+v^- cell is $|T^u|$. If one has already been picked, then the remaining chance of picking a second one becomes $(|T^u| - 1)/(N - 1)$. In total, we can write the probability of randomly selecting two u^+v^- cells or two u^-v^+ cells as

$$p_{uu} = \frac{|T^u|(|T^u| - 1)}{N(N - 1)} \quad \text{and} \quad p_{vv} = \frac{|T^v|(|T^v| - 1)}{N(N - 1)}. \tag{65}$$

Combined, the PCFs measure the ratios of u^+v^- or u^-v^+ cell pairs within every possible distance normalized by the probability of finding these cell pairs, i.e.

$$\rho_u(k) = \frac{r_{uu}(k)}{p_{uu}} = \frac{|S_k^u|N(N - 1)}{|S_k||T^u|(|T^u| - 1)}, \tag{66}$$

$$\rho_v(k) = \frac{r_{vv}(k)}{p_{vv}} = \frac{|S_k^v|N(N - 1)}{|S_k||T^v|(|T^v| - 1)}. \tag{67}$$

For a uniformly distributed amount of u^+v^- or u^-v^+ cells, the correlation function returns a value close to 1 for every cell distance k. Consequently, deviations from 1 yield information about how much more or fewer equal cell pairs are found in certain ranges.

5 Numerical results

In this section, we present the numerical solutions of (18). The explicit Euler method is used to solve the ODE until a steady state is reached. We consider two different types of signaling. Paracrine signals that exhibit low diffusivity can be described by a nearest neighbor signal. For larger diffusivities, the signal disperses throughout the tissue such that its intensity decreases with the distance traveled.

5.1 Nearest neighbor signaling

5.1.1 Signal construction

A signal that is secreted by one cell and diffuses slowly throughout the tissue will likely end up only affecting neighboring cells. Similar to Bessonnard et al. (2014), Stanoev et al. (2021), we investigate a signal that gets activated by u and depends on the neighboring cells. However, rather than investigating a time resolved signal, we consider it only as an instantaneous response such that

$$s_i = \frac{1}{|N_G(i)|} \sum_{j \in N_G(i)} u_j. \tag{68}$$

Here, we used the notation $N_G(i)$ from graph theory to denote the neighbors of vertex i in the graph G. We can also write the whole signal in terms of an adjacency matrix. For (68), this matrix is

$$A = (A_{i,j})_{i,j=1,\ldots,M}, \text{ with } A_{i,j} = \begin{cases} \frac{1}{|N_G(i)|} & \text{if } j \in N_G(i) \\ 0 & \text{if } j \notin N_G(i) \end{cases}. \tag{69}$$

The signal can ultimately be written as $s = Au$. From the steady state (24) we know $u_i = 0$ for some of the cells in a heterogeneous tissue. Therefore, the minimum of the signal will also be 0. The non-zero steady state has a rough upper bound, hence

$$u_i = \frac{r_u}{\gamma_u} - \frac{1 + \eta_s s_i}{\eta_u} < \frac{r_u}{\gamma_u}. \tag{70}$$

Therefore, the maximum signal also obeys

$$\max_i s_i = \max_i \left(\frac{1}{|N_G(i)|} \sum_{j \in N_G(i)} u_j \right) < \frac{1}{|N_G(i)|} \sum_{j \in N_G(i)} \frac{r_u}{\gamma_u} = \frac{r_u}{\gamma_u}. \tag{71}$$

Using parameter combinations, such that

$$\frac{r_u}{\gamma_u} \gg \frac{1 + \eta_s \frac{r_u}{\gamma_u}}{\eta_u}, \tag{72}$$

transforms the upper bound into a proper estimate of the signal values, such that we can conclude

$$\min_i s_i = 0 \quad \text{and} \quad \max_i s_i \approx \frac{r_u}{\gamma_u}. \tag{73}$$

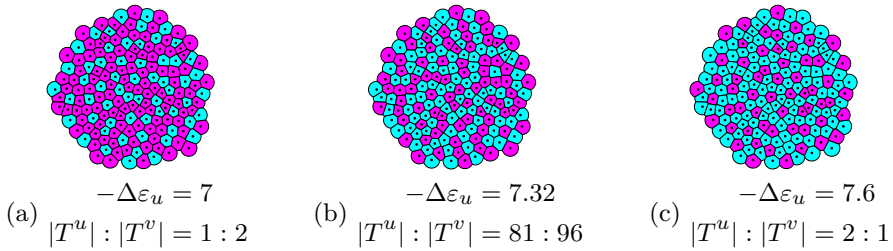Hence, the stability interval can be approximated by

🖄 Springer

(a) $\quad -\Delta\varepsilon_u = 7$
$\quad |T^u| : |T^v| = 1 : 2$

(b) $\quad -\Delta\varepsilon_u = 7.32$
$\quad |T^u| : |T^v| = 81 : 96$

(c) $\quad -\Delta\varepsilon_u = 7.6$
$\quad |T^u| : |T^v| = 2 : 1$

Fig. 5 Checkerboard pattern for three different ratios of u^+v^- and u^-v^+ cells. The coloring uses the cell's expression levels for v. High v expressions are colored in magenta, low v expressions (high u) in cyan (color figure online)

$$-\Delta\varepsilon_v + \ln\left(\frac{r_v\gamma_u}{r_u\gamma_v}\right) < -\Delta\varepsilon_u < -\Delta\varepsilon_v + \ln\left(1 + e^{-\Delta\varepsilon_s - \Delta\varepsilon_{vs}}\frac{r_u}{\gamma_u}\right) + \ln\left(\frac{r_v\gamma_u}{r_u\gamma_v}\right).$$
(74)

5.1.2 Pattern formation

Models of cell differentiation characterized by lateral inhibition tend to form an approximate checkerboard pattern of cells (Collier et al. 1996) with a trend towards alternating cell types wherever possible. In fact, the term "lateral inhibition" comes from the fact that cells of a primary cell fate prevent cells in the environment from adopting the same fate. Despite the name, the signal between neighboring cells in Collier et al. (1996) is activating rather than inhibiting. Our model differs by the inclusion of mutual inhibition and auto-activation. Thus, the goal in this section is to show that our model is still capable of forming checkerboard patterns. The parameter values and initial conditions used in any of the following simulations can be found in Table S2. The remaining energy difference $-\Delta\varepsilon_u$ is varied based on (56) to influence the cell type ratio. In the resulting cell fate pattern, u^+v^- cells mostly avoid other u^+v^- cells in their neighborhood as much as the given proportion enables them to do so (Fig. 5, see Fig. S1 for temporal evolution). Increasing $-\Delta\varepsilon_u$ increases the proportions of u^+v^- cells throughout the tissue. This results in more and more u^+v^- cells with neighbors of equal type. Increasing the proportions even further leads to the opposite effect of u^-v^+ cells trying to avoid being neighbored to cells of the same type. In total, both cell types try to avoid cells of equal type in their neighborhood as much as the proportions and the geometry of the tissue allows. In a regular 8×8 grid with, this would resemble a checkerboard. Hence, the term checkerboard pattern.

5.1.3 Cell type proportions

In some biological systems, it might be crucial to generate cell types in precise proportions like in the mouse embryo (Saiz et al. 2016, 2020). Hence, we are interested in exploring the capabilities of the model to create certain proportions. The range of possible cell type proportions can be found in the stability interval (56). For the parameter combinations chosen in this study, we get

Fig. 6 Simulated cell type proportions for 20 equidistant values of $-\Delta\varepsilon_u$ spanning over the stability interval (56). Cell proportions for u^+v^- are colored in cyan, u^-v^+ in magenta
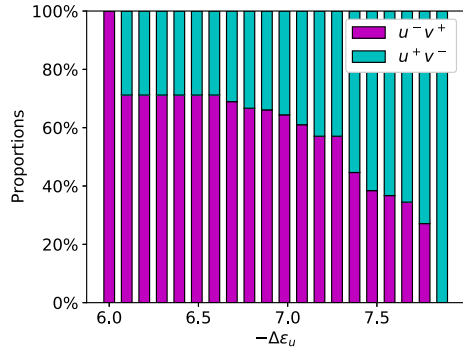
$$\frac{1 + \eta_s \frac{r_u}{\gamma_u}}{\eta_u} \leq 0.0043 \ll 0.1 = \frac{r_u}{\gamma_u}. \tag{75}$$

Hence, our approximation for the stability interval (74) is valid and yields the following parameter restrictions for the heterogeneous steady states:

$$\eta_u \in (403.43, 2606.08) \qquad \Longleftrightarrow \qquad -\Delta\varepsilon_u \in (6, 7.87). \tag{76}$$

The various cell type proportions (Fig. 6) were simulated by dividing the bounding interval (76) into 20 equidistant values for $-\Delta\varepsilon_u$. The simulation results underline the result of the stability analysis. At the left and right boundaries, we achieve homogeneity. In between, increasing $-\Delta\varepsilon_u$ yields a monotonous transition from only u^-v^+ to only u^+v^- cells. The boundary regions suggest that proportions with about 73% of one cell type and 27% of the other are the maximum and minimum cell proportions achievable before reaching homogeneity. An analytical analysis of the relation of the cell type proportions and the parameter $-\Delta\varepsilon_u$ reveals why these jumps occur. Focusing again on a single cell in the tissue, we already identified the tipping point of the cell's fate via Eq. (29). Deviating from $s = s^*$ to $s > s^*$ will increase the binding probability for v, tipping its fate towards u^-v^+. Analogously, $s < s*$ will lead to u^+v^-. By definition, s_i is the mean of a cells neighboring u_j values. Assuming the neighbors to be in steady state and using the steady state approximation $u_i \approx r_u/\gamma_u$, the signal can be written as a fraction

$$s_i = \frac{l_i}{|N_G(i)|} \frac{r_u}{\gamma_u}, \qquad l_i \in \{0, ..., |N_G(i)|\}, \tag{77}$$

where l_i denotes the number of u^+v^- cells adjacent to cell i. From this, we can determine the maximum number of u^+v^- cells in a neighborhood for the cell to still adopt the fate u^+v^-. Therefore, we replace s_i with s^* and solve the equation for l_i to find

$$l_i = |N_G(i)| \frac{\gamma_v}{r_v} \frac{\eta_u - \eta_v}{\eta_v \eta_s \eta_{vs}}. \tag{78}$$

Since we are looking for a natural number, the final result is

$$l^{\max} := \left\lfloor |N_G(i)| \frac{\gamma_v}{r_v} \frac{\eta_u - \eta_v}{\eta_v \eta_s \eta_{vs}} \right\rfloor. \tag{79}$$

Here, $\lfloor x \rfloor$ describes the floor function, i.e. the nearest lower integer of a number x. Small differences between energy coefficients $\eta_u = \eta_v + \delta$ with $\delta > 0$ being small, will lead to $l^{\max} = 0$. Therefore, a single u^+v^- cell will have no neighbor of equal type. At the same time, cells without any received signal, i.e. $s_i = 0$ will adopt u^+v^- fate (Fig. 2). In conclusion, a cell surrounded only by u^-v^+ cells will adopt u^+v^- fate, whereas a cell with a single u^+v^- in its neighborhood has to adopt u^-v^+ fate. On an ideal hexagonal grid, i.e. each cell has exactly six neighbors, an ideal arrangement would amount to $1/3$ of the cells being u^+v^-. This estimate nearly fits the simulated proportion jumps of 27% at both ends. An exact number cannot be determined, as the number of neighbors varies from cell to cell with an average of 5.5 ± 1000000 neighbors. Further increases of η_u only lead to discrete increases of $l^{\max}$, explaining the different jumps in cell type proportions.

5.2 Distance-based signaling

5.2.1 Signal construction

Motivated by recent studies of long ranging paracrine signaling (Fiorentino and Scialdone 2022; Stanoev et al. 2021) we investigate the effect of a distance-based signaling on the pattern formation and cell type proportion. Depending on how a signal disperses in space, not only directly neighboring cells can have an impact on a cell's fate. It is possible, that the collective effect of cells that are further away might also influence its fate decision. Again, the secreted signal of a cell is activated by u_i. We define the received signal s_i as the weighted sum of secreted signals over all other cells and obtain

$$s_i = \left(\sum_{j \neq i} s_j q^{d_{ij}-1} \right) \bigg/ \left(\max_k \sum_{j \neq k} q^{d_{kj}-1} \right), \qquad q \in [0, 1]. \tag{80}$$

Here, we use the distances d_{ij} from our cell graph. The weights $q^{d_{ij}-1}$ define the fraction of the signal that gets transported from cell to cell. Let e.g. $q = 0.1$, then second nearest neighbors of a cell receive only 10% of the signal of the direct neighbors (Fig. 7). The denominator in (80) is used for normalization. It describes the weights of the cell that gets the highest possible signaling weights. In a perfectly arranged circular tissue, this would be the cell right in its center due to the mean of cell distances d_{ij} being lower. The dispersion parameter q enables us to describe the transition from a
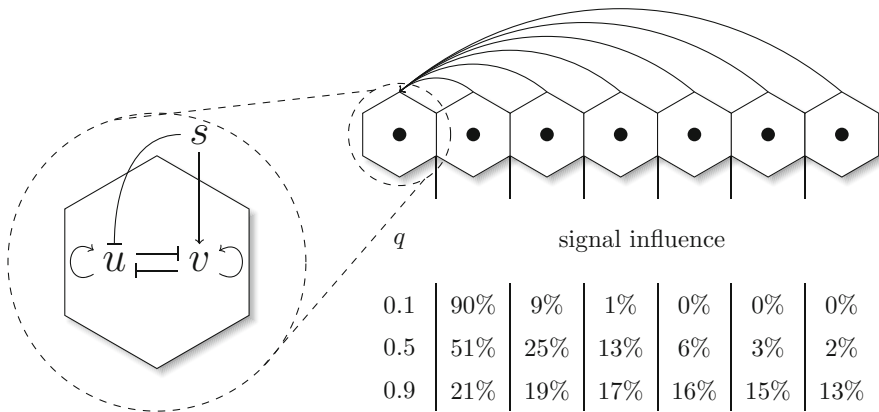
Fig. 7 Illustration of the GRN represented by our model as well as a representative example of the signaling in a one-dimensional cell line. Inside the cell, u and v mutually inhibit each other. Additionally, v gets activated by an extracellular signal, whereas u is inhibited by the same. The signal received by the first cell on the left of the line is the sum of all cell–cell communication between one cell and any other cell in the system. The table highlights how much each cell contributes to the received signal for different dispersions $q \in \{0.1, 0.5, 0.9\}$. Percentages are rounded to the nearest integer

direct neighbor signal to an equally dispersed signal. For $q = 0$, the weights become

$$q^{d_{ij}-1} = 0^{d_{ij}-1} = \begin{cases} 1, & \text{for } d_{ij} = 1 \\ 0, & \text{for } d_{ij} > 1 \end{cases}. \tag{81}$$

Hence, the weights for all cells that are not directly in contact with the respective cell are 0 and we obtain a mechanism similar to the local signal (68). Alternatively, $q = 1$ yields

$$q^{d_{ij}-1} = 1^{d_{ij}-1} = 1. \tag{82}$$

This describes the case of every cell having the same impact on other cells independent of the distance between them. In summary, there is a continuous transition from a next neighbor signal at $q = 0$, through a distance-based global signal for $q \in [0, 1]$, to an evenly distributed signal at $q = 1$. In matrix representation we get

$$A = (A_{i,j})_{i,j=1,\dots,M} \text{ with } A_{i,j} = \begin{cases} aq^{d_{ij}-1} & \text{if } i \neq j \\ 0 & \text{if } i = j \end{cases} \tag{83}$$

and the normalization factor

$$a = \left(\max_k \sum_{l \neq k} q^{d_{kl}-1} \right)^{-1}. \tag{84}$$

For the estimation of the stability interval, we again use the upper bound $u_i < r_u/\gamma_u$, such that

$$s_i < \frac{r_u}{\gamma_u} \left(\sum_{j \neq i} q^{d_{ij}-1} \right) \bigg/ \left(\max_k \sum_{j \neq k} q^{d_{kj}-1} \right) \tag{85}$$

$$\leq \frac{r_u}{\gamma_u} \left(\max_k \sum_{j \neq k} q^{d_{kj}-1} \right) \bigg/ \left(\max_k \sum_{j \neq k} q^{d_{kj}-1} \right) = \frac{r_u}{\gamma_u}. \tag{86}$$

At this point, we realize that the estimation follows the exact same procedure as before, leading to (74). It should be mentioned, that the choice of (80) is not based on a physical foundation, but is simply a mathematical construct that could be easily unified with the result of the stability analysis but still allows to investigate the concept of different signaling ranges.

5.2.2 Pattern formation

We want to investigate the effect of the distance-based signal on the formation of the patterns. Therefore, we showcase nine simulation results of organoids with different cell type proportions and different signal dispersions (Fig. 8 and Fig. S2-S4). The patterns generated for $q = 0.1$ can mostly be considered of the checkerboard type. In contrast to the averaged nearest neighbor signal, the signal in this case is not averaged over the number of neighbors. Cells at the boundary typically have three to four neighboring cells, whereas cells in the bulk area have a mean of six neighbors. Therefore, cells at the boundary will potentially not be able to get the same amount of signal as cells in the bulk area. Such boundary effects are representative of fixed size systems such as embryoid bodies or organoids. Furthermore, they are likely to occur at tissue-tissue or tissue-cavity interfaces within developing embryos.

The received signal however, is the deciding factor with regard to the cell fate decision in our model. The low amounts of signal received at the boundary make them more likely to adopt the u^+v^- fate. As q increases, we see a higher accumulation of u^+v^- cells near the boundary with a slight clustering behavior in the bulk. For $q = 0.9$, the signal disperses strongly enough to generate an engulfing pattern, where u^-v^+ cells are completely surrounded by u^+v^- cells. Varying the proportions of u^+v^- cells via $-\Delta\varepsilon_u$ has a different effect based on the signal dispersion q. For low q and increasing u^+v^- proportions, we find a ring of u^+v^- cells engulfing the remaining checkerboard pattern. For medium to large q this effect is more strongly pronounce with the formation of several layers of u^+v^- cells engulfing the tissue.

The pattern formation with respect to q can be quantified using the PCFs for both u^+v^- and u^-v^+ cells (Fig. 9). For comparison, we used a bisection on the stability interval to find values for $-\Delta\varepsilon_u$ that lead to a ratio of 89 : 88 u^+v^- and u^-v^+ cells for every single q. We discover that an increase in q leads to a decrease of ρ_v for large distances, i.e. less and less pairs of u^-v^+ cells pairing in the boundary regions. Simultaneously, it increases for small distances due to the cells accumulating in the center. For ρ_u, we see a slight increase for large q for small distances and a
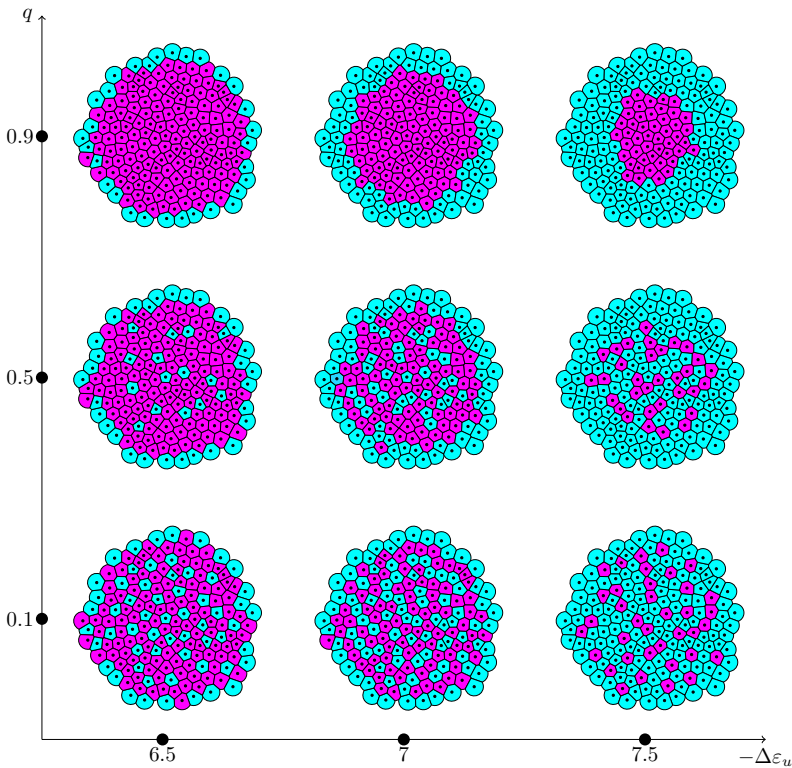
Fig. 8 Different patterns generated by the model on a tissue geometry with 177 cells. Colors depict the values of v_i in steady state. High values of v_i correspond to low values in u_i and vice-versa, i.e. cyan and magenta represent u^+v^- and u^-v^+ cells, respectively. From left to right, $-\Delta\varepsilon_u$ increases. From bottom to top, the dispersion q increases (color figure online)

tremendous one for large distances for all q. The slight increase at small distances comes from the fact that the u^+v^- cells arrange in layers at the boundary. The values for intermediate distances slightly decrease as the corresponding regions become more and more devoid of u^-v^+ pairs. In conclusion, a distance-based signal according to (80) generates patterns ranging from checkerboard to engulfing by increasing the dispersion parameter q. Additionally, the PCFs capture the characteristics of these patterns, making it a powerful tool for pattern identification and comparison.

5.2.3 Cell type proportion

For different dispersion parameter values q, the proportions of u^-v^+ show a monotonous decrease with increasing energy difference $-\Delta\varepsilon_u$ (Fig. 10). For low values of q, the proportions show some similarities to the local model due to individual larger jumps (Fig. 10a). These jumps become less pronounced for medium (Fig. 10b) and high dispersions (Fig. 10c). Altogether, we have established full control over the cell type proportions.
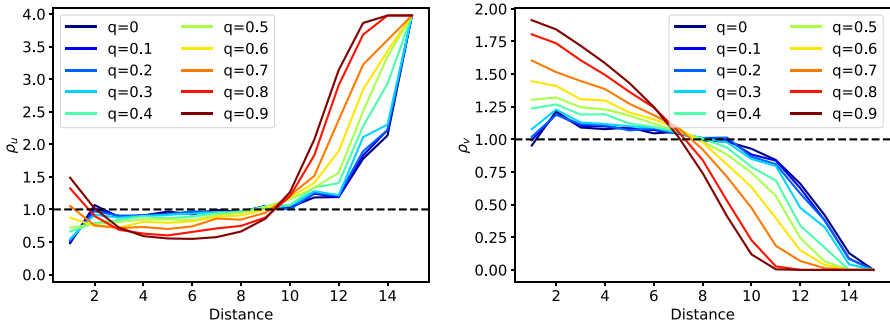
🖄 Springer

Fig. 9 PCFs for u^+v^- cells (left) and u^-v^+ cells (right) for different dispersion parameters q. Any PCF represents a tissue with a ratio of $u^+v^-{:}u^-v^+ = 88 : 89$. The dashed black line at 1 resembles the PCF values of an ideal uniform distribution of two different cell types. If values lie above 1, this means there are more pairs found at that distance. Consequently, values below 1 resemble fewer pairs
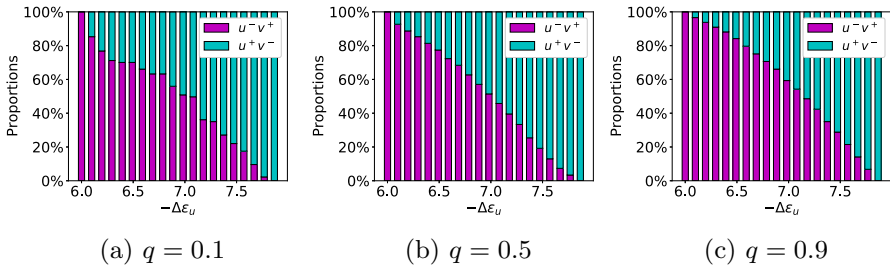

Fig. 10 Simulated cell type proportions with respect to $-\Delta\varepsilon_u$. Simulations were performed by dividing the stability interval for $-\Delta\varepsilon_u$ into 20 equidistant values. Dispersion parameter q increases from **(a)** to **(c)** resulting in different scenarios

6 Discussion

In this study, we have derived and analyzed a model that allows us to generate cell differentiation patterns based on a system of mutual inhibition of two TFs, auto-activation and cell–cell communication. The model was thoroughly analyzed and simulated patterns were characterized.

6.1 Derivation of the model from statistical mechanics

Statistical mechanics has already proven its usefulness in biological model systems like ion channel opening and closing as well as oxygen hemoglobin binding (Garcia et al. 2011). These ideas have further been investigated for transcriptional regulation and were successfully applied for a wide variety of examples (Bintu et al. 2005a, b). To our knowledge, cell fate decision models have not been combined with statistical mechanics to date. We derived a specific model based on two mutually inhibiting TFs u and v with auto-activation and an external signal inhibiting u and activating v. Assuming that auto-activation is the dominant factor in transcriptional regulation, we assume that RNA polymerase binding corresponds to the binding of u and v,

respectively. Based on this, we were able to derive binding probabilities of RNA polymerase to the respective promoter. A system of ordinary differential equations was generated by combining these probabilities with constant production rates and exponential decay. As long as the auto-activation remains unchanged, minor changes in the GRN such as the removal of either the signal activation or the signal inhibition can still be managed by adjusting the equations accordingly.

6.2 Analysis of the model allows accurate determination of the stability of heterogeneous steady states

On the single cell level, we identified that the received signal determines the fate of a cell. There is a critical value of this signal, such that the cell will adopt u^-v^+ fate if this value is undercut, or u^+v^- fate if the value is exceeded. This leads to the signal being the relevant factor of the switching behavior in this system. This describes a different point of view compared to systems that utilize differences in initial conditions to generate a cell fate switch (Cherry and Adler 2000; Huang et al. 2007). At the same time, models that incorporate a signal dependency, have not yet been analyzed in such great detail (Bessonnard et al. 2014; Stanoev et al. 2021; Tosenberger et al. 2017). Exact expressions for all possible steady states were derived. A stability analysis enabled us to identify parameter values, such that only the states corresponding to u^+v^- and u^-v^+ fates are stable. Thus, we were able to limit the system to these two cell fates. On the level of multiple cells, we found analytical expressions of parameter bounds guaranteeing heterogeneous steady states. This means that within these bounds the pattern created by the system will always be a mixture of two different cell types. In conclusion, we have provided the necessary analytical tools to guarantee the generation of heterogeneous patterns of two different cell types.

6.3 Averaged nearest neighbor signaling leads to checkerboard patterns

In some biological systems, cell communication is hypothesized to be limited to direct neighbors. An example for this is the lateral inhibition of Delta and Notch in epithelial tissue of *Drosophila*, which has been studied in great detail (Collier et al. 1996). A different example is found in the preimplantation development of the mouse embryo, where TFs NANOG and GATA6 decide the fate of cells in the inner cell mass. Different computational studies have investigated the effects of activation by an external signal in this biological system (Bessonnard et al. 2014; Mot et al. 2016; Tosenberger et al. 2017). A great common feature in all of these systems is the formation of checkerboard patterns, i.e. patterns in which cells of one type minimize the number of equal neighbors. Fittingly, we also found this type of pattern in our simulations using an averaged nearest neighbor signaling. We took this one step further and analyzed the possible cell type proportions one can create using this model. An analytical expression for the maximum number of equal cell types in a cell's neighborhood tells us that the cell type proportions are highly linked to the average number of neighboring cells in the system. In our 2D simulations cell type proportions below 30% and above 70% are not possible.

6.4 Distance-based signaling enables a range of patterns from checkerboard to engulfing

In addition to the nearest neighbor signal, we investigated the effects of a signal that is capable of being dispersed throughout the tissue. This global cell–cell communication enables a range of patterns. From two cell types in a checkerboard like arrangement to one cell type engulfing the other depending on the signal dispersion. The introduced dispersion parameter q allows us to artificially vary between a signal that only reaches the neighboring cells and a signal that spreads evenly in the tissue. Simulations have shown that for low signal dispersion u^+v^- and u^-v^+ cells tend to avoid being adjacent to the same cell type, hence we again recovered the checkerboard pattern. Furthermore, when increasing the signal dispersion, u^+v^- cells accumulate more at the boundary such that overall larger clusters of equal cell types are formed. High signal dispersion leads to an ideal segregation of cells with u^+v^- engulfing u^-v^+ cells. Engulfing patterns are often believed to be the result of differential adhesion of two cell types. Indeed, it has already been demonstrated that the minimization of the energy as a function of differential adhesion leads to this type of engulfing (Emily and François 2007). Not only have we found an alternative way to generate these patterns, but at the same time we were able to unify the formation of both checkerboard and engulfing patterns under the notion of differently dispersing signals.

6.5 Biological examples for the different patterns

The lateral inhibition principle exemplified by the Notch-Delta signalling pathway leads to alternating fates between neighboring cells. At the multicellular level, this results in a checkerboard pattern. Different systems show patterns of longer spatial scales of local clusters such as the developing mouse neural tissue (Hawley et al. 2022) or in vitro stem cell differentiation in embryoid bodies (White et al. 2013) and ICM organoids. Completely engulfing patterns have been observed as transient patterns in differentiating embryoid bodies (White et al. 2013) and ICM organoids that have been cultured for a sufficiently long time (Mathew et al. 2019). Partly engulfing patterns arise in different embryos including mammalian, e.g. mouse or human (Płusa and Piliszek 2020), and fish, e.g. zebrafish (Gilbert 2014). The relevance of our model results to these different systems has to be evaluated based on careful comparison of the arising patterns and underlying GRNs.

6.6 Conclusion

We have provided a new model to describe transcriptional regulation for a system of mutually exclusive TFs. Furthermore, the model was analyzed in great detail with respect to parameters and stability. The model was extended by signaling mechanisms describing the cell–cell communication. The local and global signaling obey a simple mathematical rule depending on the number of cells it has to travel across in order to reach its destination. A detailed description of the signaling transport mechanism, possibly including diffusion and advection mechanisms, provides room for further

research. Additionally, signal production and uptake of cells play a crucial role in how effective different means of signal transport might be. Another perspective can be achieved by incorporating cell growth and cell division into the model and analyzing their effect on the resulting patterns. With this in mind, our study paves the way for numerous subsequent studies regarding signal-based pattern formation in developmental systems.

Code Availability   Not applicable.

Declarations

Conflict of interest   The authors have no competing interests to declare that are relevant to the content of this article.

Ethical approval   No Experiments have been performed.

Informed consent   No Experiments have been performed.

References

Bessonnard S, De Mot L, Gonze D, Barriol M, Dennis C, Goldbeter A, Dupont G, Chazaud C (2014) Gata6, Nanog and Erk signaling control cell fate in the inner cell mass through a tristable regulatory network. Development 141(19):3637–3648. https://doi.org/10.1242/dev.109678

Binder BJ, Simpson MJ (2013) Quantifying spatial structure in experimental observations and agent-based simulations using pair-correlation functions. Phys Rev E 88:022705. https://doi.org/10.1103/PhysRevE.88.022705

Bintu L, Buchler NE, Garcia HG, Gerland U, Hwa T, Kondev J, Phillips R (2005) Transcriptional regulation by the numbers: models. Curr Opin Genet Dev 15(2):116–124. https://doi.org/10.1016/j.gde.2005.02.007

Bintu L, Buchler NE, Garcia HG, Gerland U, Hwa T, Kondev J, Kuhlman T, Phillips R (2005) Transcriptional regulation by the numbers: applications. Curr Opin Genet Dev 15(2):125–135. https://doi.org/10.1016/j.gde.2005.02.006

Chen JS, Gumbayan AM, Zeller RW, Mahaffy JM (2014) An expanded notch-delta model exhibiting long-range patterning and incorporating MicroRNA regulation. PLOS Comput Biol 10(6):1003655. https://doi.org/10.1371/journal.pcbi.1003655

Cherry JL, Adler FR (2000) How to make a biological switch. J Theor Biol 203(2):117–133. https://doi.org/10.1006/jtbi.2000.1068

Cohen M, Georgiou M, Stevenson NL, Miodownik M, Baum B (2010) Dynamic filopodia transmit intermittent delta-notch signaling to drive pattern refinement during lateral inhibition. Dev Cell 19(1):78–89. https://doi.org/10.1016/j.devcel.2010.06.006

Collier JR, Monk NAM, Maini PK, Lewis JH (1996) Pattern formation by lateral inhibition with feedback: a mathematical model of delta-notch intercellular signalling. J Theor Biol 183(4):429–446. https://doi.org/10.1006/jtbi.1996.0233

de Joussineau C, Soulé J, Martin M, Anguille C, Montcourrier P, Alexandre D (2003) Delta-promoted filopodia mediate long-range lateral inhibition in Drosophila. Nature 426(6966):555–559. https://doi.org/10.1038/nature02157

Dirk R, Fischer JL, Schardt S, Ankenbrand MJ, Fischer SC (2022) Recognition and reconstruction of cell differentiation patterns with deep learning. arXiv. https://doi.org/10.48550/ARXIV.2212.10058. arXiv:2212.10058

Emily M, François O (2007) A statistical approach to estimating the strength of cell-cell interactions under the differential adhesion hypothesis. Theor Biol Med Model 4:37. https://doi.org/10.1186/1742-4682-4-37

Fiorentino J, Scialdone A (2022) The role of cell geometry and cell-cell communication in gradient sensing. PLOS Comput Biol 18(3):1–22. https://doi.org/10.1371/journal.pcbi.1009552

Garcia HG, Kondev J, Orme N, Theriot JA, Phillips R (2011) Thermodynamics of biological processes. Methods Enzymol 492:27–59. https://doi.org/10.1016/B978-0-12-381268-1.00014-8

Gerland U, Moroz JD, Hwa T (2002) Physical constraints and functional characteristics of transcription factor-DNA interaction. Proc Natl Acad Sci 99(19):12015–12020. https://doi.org/10.1073/pnas.192693599

Gilbert SF (2014) Developmental Biology/Scott F. Gilbert., 10th edn. Sinauer Associates, Sunderland, Mass

Hawley J, Manning C, Biga V, Glendinning P, Papalopulu N (2022) Dynamic switching of lateral inhibition spatial patterns. J R Soc Interface 19(193):20220339. https://doi.org/10.1098/rsif.2022.0339

Heitzler P, Simpson P (1991) The choice of cell fate in the epidermis of drosophila. Cell 64(6):1083–1092. https://doi.org/10.1016/0092-8674(91)90263-X

Huang S, Guo Y-P, May G, Enver T (2007) Bifurcation dynamics in lineage-commitment in bipotent progenitor cells. Dev Biol 305(2):695–713. https://doi.org/10.1016/j.ydbio.2007.02.036

Liebisch T, Drusko A, Mathew B, Stelzer EHK, Fischer SC, Matthäus F (2020) Cell fate clusters in ICM organoids arise from cell fate heredity and division: a modelling approach. Sci Rep 10(1):22405. https://doi.org/10.1038/s41598-020-80141-3

Mathew B, Muñoz-Descalzo S, Corujo-Simon E, Schröter C, Stelzer EHK, Fischer SC (2019) Mouse ICM organoids reveal three-dimensional cell fate clustering. Biophys J 116(1):127–141. https://doi.org/10.1016/j.bpj.2018.11.011

Mitsui K, Tokuzawa Y, Itoh H, Segawa K, Murakami M, Takahashi K, Maruyama M, Maeda M, Yamanaka S (2003) The homeoprotein Nanog is required for maintenance of pluripotency in mouse epiblast and es cells. Cell 113(5):631–642. https://doi.org/10.1016/S0092-8674(03)00393-3

Morris SA, Teo RTY, Li H, Robson P, Glover DM, Zernicka-Goetz M (2010) Origin and formation of the first two distinct cell types of the inner cell mass in the mouse embryo. Proc Natl Acad Sci USA 107(14):6364–6369. https://doi.org/10.1073/pnas.0915063107

Morris SA, Graham SJL, Jedrusik A, Zernicka-Goetz M (2013) The differential response to Fgf signalling in cells internalized at different times influences lineage segregation in preimplantation mouse embryos. Open Biol 3(11):130104. https://doi.org/10.1098/rsob.130104

Mot LD, Gonze D, Bessonnard S, Chazaud C, Goldbeter A, Dupont G (2016) Cell fate specification based on tristability in the inner cell mass of mouse blastocysts. Biophys J 110(3):710–722. https://doi.org/10.1016/j.bpj.2015.12.020

Nichols J, Silva J, Roode M, Smith A (2009) Suppression of Erk signalling promotes ground state pluripotency in the mouse embryo. Development 136(19):3215–3222. https://doi.org/10.1242/dev.038893

Nissen SB, Perera M, Gonzalez JM, Morgani SM, Jensen MH, Sneppen K, Brickman JM, Trusina A (2017) Four simple rules that are sufficient to generate the mammalian blastocyst. PLOS Biol 15(7):1–30. https://doi.org/10.1371/journal.pbio.2000737

Płusa B, Piliszek A (2020) Common principles of early mammalian embryo self-organisation. Development 147(14):dev183079. https://doi.org/10.1242/dev.183079

Raina D, Bahadori A, Stanoev A, Protzek M, Koseska A, Schröter C (2021) Cell-cell communication through FGF4 generates and maintains robust proportions of differentiated cell types in embryonic stem cells. Development. https://doi.org/10.1242/dev.199926

Revell C, Blumenfeld R, Chalut KJ (2019) Force-based three-dimensional model predicts mechanical drivers of cell sorting. Proc R Soc B Biol Sci 286(1895):20182495. https://doi.org/10.1098/rspb.2018.2495

Saiz N, Williams KM, Seshan VE, Hadjantonakis A-K (2016) Asynchronous fate decisions by single cells collectively ensure consistent lineage composition in the mouse blastocyst. Nat Commun 7(1):13463. https://doi.org/10.1038/ncomms13463

Saiz N, Mora-Bitria L, Rahman S, George H, Herder JP, Garcia-Ojalvo J, Hadjantonakis A-K (2020) Growth-factor-mediated coupling between lineage size and cell fate choice underlies robustness of mammalian development. eLife 9:56079. https://doi.org/10.7554/eLife.56079

Schmitz A, Fischer SC, Mattheyer C, Pampaloni F, Stelzer EHK (2017) Multiscale image analysis reveals structural heterogeneity of the cell microenvironment in homotypic spheroids. Sci Rep 7(1):43693. https://doi.org/10.1038/srep43693

Schrode N, Saiz N, Di Talia S, Hadjantonakis A-K (2014) Gata6 levels modulate primitive endoderm cell fate choice and timing in the mouse blastocyst. Dev cell 29(4):454–467. https://doi.org/10.1016/j.devcel.2014.04.011

Schröter C, Rué P, Mackenzie JP, Martinez Arias A (2015) FGF/MAPK signaling sets the switching threshold of a bistable circuit controlling cell fate decisions in embryonic stem cells. Development 142(24):4205–4216. https://doi.org/10.1242/dev.127530

Stanoev A, Schröter C, Koseska A (2021) Robustness and timing of cellular differentiation through population-based symmetry breaking. Development 148(3):dev197608. https://doi.org/10.1242/dev.197608

Sternberg PW (1993) Falling off the knife edge. Curr Biol 3(11):763–765. https://doi.org/10.1016/0960-9822(93)90025-J

Torii KU (2012) Two-dimensional spatial patterning in developmental systems. Trends Cell Biol 22(8):438–446

Tosenberger A, Gonze D, Bessonnard S, Cohen-Tannoudji M, Chazaud C, Dupont G (2017) A multiscale model of early cell lineage specification including cell division. NPJ Syst Biol Appl 3(1):16. https://doi.org/10.1038/s41540-017-0017-0

White DE, Kinney MA, McDevitt TC, Kemp ML (2013) Spatial pattern dynamics of 3d stem cell loss of pluripotency via rules-based computational modeling. PLOS Comput Biol 9(3):1–12. https://doi.org/10.1371/journal.pcbi.1002952

Yamanaka Y, Lanner F, Rossant J (2010) FGF signal-dependent segregation of primitive endoderm and epiblast in the mouse blastocyst. Development 137(5):715–724. https://doi.org/10.1242/dev.043471

ⓐ Springer

Terms and Conditions

Springer Nature journal content, brought to you courtesy of Springer Nature Customer Service Center GmbH ("Springer Nature").

Springer Nature supports a reasonable amount of sharing of research papers by authors, subscribers and authorised users ("Users"), for small-scale personal, non-commercial use provided that all copyright, trade and service marks and other proprietary notices are maintained. By accessing, sharing, receiving or otherwise using the Springer Nature journal content you agree to these terms of use ("Terms"). For these purposes, Springer Nature considers academic use (by researchers and students) to be non-commercial.

These Terms are supplementary and will apply in addition to any applicable website terms and conditions, a relevant site licence or a personal subscription. These Terms will prevail over any conflict or ambiguity with regards to the relevant terms, a site licence or a personal subscription (to the extent of the conflict or ambiguity only). For Creative Commons-licensed articles, the terms of the Creative Commons license used will apply.

We collect and use personal data to provide access to the Springer Nature journal content. We may also use these personal data internally within ResearchGate and Springer Nature and as agreed share it, in an anonymised way, for purposes of tracking, analysis and reporting. We will not otherwise disclose your personal data outside the ResearchGate or the Springer Nature group of companies unless we have your permission as detailed in the Privacy Policy.

While Users may use the Springer Nature journal content for small scale, personal non-commercial use, it is important to note that Users may not:

1. use such content for the purpose of providing other users with access on a regular or large scale basis or as a means to circumvent access control;

2. use such content where to do so would be considered a criminal or statutory offence in any jurisdiction, or gives rise to civil liability, or is otherwise unlawful;

3. falsely or misleadingly imply or suggest endorsement, approval , sponsorship, or association unless explicitly agreed to by Springer Nature in writing;

4. use bots or other automated methods to access the content or redirect messages

5. override any security feature or exclusionary protocol; or

6. share the content in order to create substitute for Springer Nature products or services or a systematic database of Springer Nature journal content.

In line with the restriction against commercial use, Springer Nature does not permit the creation of a product or service that creates revenue, royalties, rent or income from our content or its inclusion as part of a paid for service or for other commercial gain. Springer Nature journal content cannot be used for inter-library loans and librarians may not upload Springer Nature journal content on a large scale into their, or any other, institutional repository.

These terms of use are reviewed regularly and may be amended at any time. Springer Nature is not obligated to publish any information or content on this website and may remove it or features or functionality at our sole discretion, at any time with or without notice. Springer Nature may revoke this licence to you at any time and remove access to any copies of the Springer Nature journal content which have been saved.

To the fullest extent permitted by law, Springer Nature makes no warranties, representations or guarantees to Users, either express or implied with respect to the Springer nature journal content and all parties disclaim and waive any implied warranties or warranties imposed by law, including merchantability or fitness for any particular purpose.

Please note that these rights do not automatically extend to content, data or other material published by Springer Nature that may be licensed from third parties.

If you would like to use or distribute our Springer Nature journal content to a wider audience or on a regular basis or in any other manner not expressly permitted by these Terms, please contact Springer Nature at

onlineservice@springernature.com